Quantitative third-harmonic generation imaging of mouse visual cortex areas reveals correlations between functional maps and structural substrates

Research Article | Vol. 11, No. 10 / 1 October 2020 / Biomedical Optics Express 5650
Biomedical Optics EXPRESS

Quantitative third-harmonic generation imaging of mouse visual cortex areas reveals correlations between functional maps and structural substrates

MURAT YILDIRIM,[1,5] MING HU,[1] NHAT M. LE,[1,2] HIROKI SUGIHARA,[1] PETER T. C. SO,[3] AND MRIGANKA SUR[1,2,4,6]

[1]*Picower Institute for Learning and Memory, Massachusetts Institute of Technology, Cambridge, MA 02139, USA*
[2]*Department of Brain and Cognitive Sciences, Massachusetts Institute of Technology, Cambridge, MA 02139, USA*
[3]*Departments of Mechanical and Biological Engineering, Massachusetts Institute of Technology, Cambridge, MA 02139, USA*
[4]*Simons Center for the Social Brain, Massachusetts Institute of Technology, Cambridge, MA 02139, USA*
[5]*muraty@mit.edu*
[6]*msur@mit.edu*

Abstract: The structure of brain regions is assumed to correlate with their function, but there are very few instances in which the relationship has been demonstrated in the live brain. This is due to the difficulty of simultaneously measuring functional and structural properties of brain areas, particularly at cellular resolution. Here, we performed label-free, third-harmonic generation (THG) microscopy to obtain a key structural signature of cortical areas, their effective attenuation lengths (EAL), in the vertical columns of functionally defined primary visual cortex and five adjacent visual areas in awake mice. EALs measured by THG microscopy in the cortex and white matter showed remarkable correspondence with the functional retinotopic sign map of each area. Structural features such as cytoarchitecture, myeloarchitecture and blood vessel architecture were correlated with areal EAL values, suggesting that EAL is a function of these structural features as an optical property of these areas. These results demonstrate for the first time a strong relationship between structural substrates of visual cortical areas and their functional representation maps in vivo. This study may also help in understanding the coupling between structure and function in other animal models as well as in humans.

1. Introduction

Form and function are closely related in nature, and hence an important question in neuroscience is to understand the relationship between the structure and function of brain regions [1]. Cytoarchitecture [2], and myeloarchitecture [3,4] are commonly used metrics for defining structural features of the brain. Resting state or spontaneous activity [5,6], neuronal activity evoked by a sensory stimulus [7] or during behavior [8], and retinotopic mapping [9] are established metrics for defining the function of brain regions. Previous studies have suggested relationships between cytoarchitecture and function [10,11], as well as between myeloarchitecture and function of brain regions [12–14] among humans and nonhuman primates. Some of these relationships can be measured by structural and functional magnetic resonance imaging (MRI) [15]. Since the spatial resolution of MRI is on the order of 100 μm at best [16], it does not provide adequate measurement resolution for many brain regions in small animals such as mice. Furthermore, structural properties of brain tissue are easily altered ex vivo. Thus, high-resolution imaging technologies which can provide both structural and functional information in small animal model systems in vivo are needed.

#396962 https://doi.org/10.1364/BOE.396962
Journal © 2020 Received 6 May 2020; revised 26 Aug 2020; accepted 8 Sep 2020; published 16 Sep 2020

Biomedical Optics EXPRESS

Multiphoton microscopy has revolutionized neuroscience by providing subcellular resolution as well as capabilities for deep-brain imaging [17–19] in mice. However, there are limitations to both two- and three-photon microscopy with respect to maximum imaging depth, depending on signal-to-noise ratio, as well as optical properties such as scattering and absorption lengths of specific brain regions [19,20]. Several of these features are related to structural components of the cortex, such as cytoarchitecture and myeloarchitecture [21,22]. The effective attenuation length (EAL), defined as the combination of scattering and absorption lengths, provides a correlate of these structural components and is crucial for determining maximum imaging depth of any brain region for performing reliable imaging and manipulation of cells [23–25]. The most common technique to determine the EAL is by labeling blood vessels via the injection of high absorption cross-section dyes retro-orbitally in anesthetized mice [26]. However, this method assumes uniform labeling of blood vessels, as well as similar optical properties of the anesthetized and awake animal brain, and is based on both excitation and emission photons. Limitations of these assumptions will affect the precision of this technique for calculating the EAL. Due to these limitations, as well as the limited duration of the dye in the blood vessels after retro-orbital injection, alternative and more precise methods are required to characterize the EALs for multiple brain regions in the same animal.

We recently showed that the EAL can be estimated either with third-harmonic generation (THG) imaging of blood vessels and myelin fibers at 1300 nm excitation wavelength in the cortex and in the white matter, respectively, or focally ablating tissue at multiple depths in the primary visual cortex (V1) of awake mice [19]. THG imaging is a label-free three-photon microscopy technique that is sensitive to index of refraction and third order susceptibility changes [27,28]. Previous studies have shown that THG could be used to image blood vessels [19,29], neurons and their processes [30,31], and myelin [21] in the vertebrate central nervous system. Thus, THG imaging of blood vessels and myelin fibers in awake mouse brain can provide in vivo structural information. Together with accurate functional identification of brain regions, such as by using retinotopic maps, THG imaging can then be used to relate their structure to their function.

Cortical areas in the mouse brain can be broadly localized via their stereotaxic coordinates [32,33]; this method is effective for targeting large sections of cortex such as primary visual cortex (V1), motor cortex (M1), or somatosensory cortex (S1). However, this method is less accurate for targeting small functional regions, such as higher visual areas in mice (for example, the anterolateral (AL), lateromedial (LM), posteromedial (PM), anteromedial (AM), rostrolateral (RL) regions of visual cortex) as identified by widefield imaging of intrinsic optical signals [34,35] or imaging of calcium indicator activity such as GCaMP6s [36]. Primary visual cortex in mice can in some instances be colocalized with cytoarchitecture, chemoarchitecture, and myeloarchitecture features [36–38]. However, it has been difficult to find unique structural markers for these areas, and thus their identification remains solely based on retinotopy and even sign map alone. Importantly, there have been no detailed in vivo studies relating structural and functional properties of these visual areas in awake mice.

Here, we wished to examine in awake mice if functionally defined areas have different optical properties – specifically, different EALs - since we hypothesize that the EAL is a function of structural substrates such as cytoarchitecture, myeloarchitecture, and blood vessel architecture. First, we identified six visual areas through retinotopic mapping via one-photon imaging of GCaMP6s transgenic awake mice. Next, we used label-free, sub-cellular resolution three-photon microscopy to perform depth-resolved THG imaging in each area to determine their corresponding EALs in the cortex and in the white matter. We find that these EALs are unique to each area and are correlated with the retinotopic sign map of visual areas. We next analyzed the cytoarchitecture, in vivo myeloarchitecture, and blood-vessel architecture in each area to reveal their contribution on the EAL values of each visual area. The cytoarchitecture of each area allowed us to estimate their EAL values, which we found are comparable to experimental EAL values. Moreover,

Biomedical Optics EXPRESS

the orientation of blood vessels and myelin fibers in each area showed similar trends as their EAL values. Finally, we carried out ablation experiments as an alternative method to estimate EAL values that is not affected by emission wavelengths. The EALs estimated by our ablation experiments are 17% higher and strongly correlated with EAL estimates obtained with THG imaging. These characterizations increased our confidence in the use of THG imaging of blood vessels and myelin fibers as a method to estimate the EAL values in the brain. Importantly, these new results obtained by THG imaging and ablation demonstrate, for the first time, that EAL and retinotopic sign map measurements are strongly correlated, suggesting a strong relationship between the structure and function of multiple visual areas at subcellular resolution measured in awake mice.

2. Materials and methods

2.1. Custom-made three-photon system

Ultrashort laser pulses (300 fs, 400 kHz, 16 W) at 1045 nm from a pump laser (Spirit, Spectra Physics) were passed through a noncollinear optical parametric amplifier (NOPA, Spectra Physics) to obtain the excitation wavelength of 1300 nm for GCaMP6s and THG imaging. The internal compressor in NOPA could compress the Gaussian pulse width to 22 fs (which was the transform limited pulse width for a 110 nm spectral full-width half-maximum bandwidth laser pulse). Due to the dispersion in the microscope, the Gaussian pulse width on the sample was ~200 fs. In order to shorten the pulse width on the sample, a two-prism-based external compressor was built to prechirp the pulse before sending it to the microscope, reducing the pulse width to 35 fs on the sample. After pulse broadening, a delay line was used to double the repetition rate and increase the frame rate for THG imaging so that a frame rate with 512×512 pixels for a 350×350 μm^2 field of view could be increased up to 2 Hz. Power control was performed with the combination of a half-wave plate (AHWP05M-1600, Thorlabs) and a low-GDD ultrafast beamsplitter (UFBS2080, Thorlabs) with 100:1 extinction ratio. The laser beams were scanned by a pair of galvanometric mirrors (6215H, Cambridge Technologies) to image the laser spot on the back aperture of the objective using a pair of custom-designed scan and tube lenses. The emitted signal from the mouse brain was collected by a pair of collection lenses for three PMTs. GCaMP6s fluorescence signals were detected using GaAsP photomultiplier tubes (H7422A-40, Hamamatsu, Japan); THG signal was detected using a bialkali (BA) photomultiplier tube (R7600U-200). A commercially available objective with high transmission at a longer wavelength (25x, 1.05-NA, XLPN25XWMP2, Olympus) was used. Image acquisition was carried out using ScanImage (Vidrio). Imaged cells, blood vessels, and myelin fibers were located at a depth of 0-1200 μm or more below the pial surface. Laser power ranged from 0.5-50 mW at the sample depending on depth and fluorescence expression levels. Awake mice were placed on a two-axis motorized stage (MMBP, Scientifica) and the objective lens was placed on a single axis motorized stage (MMBP, Scientifica) to move in the axial direction. Mice were fixed on the stage with a sample holder, and a head mount was placed on top of the head to minimize motion artifacts during imaging.

2.2. One-photon imaging system for area segmentation in visual areas of awake mice

Widefield one-photon imaging was performed using a custom-made one-photon widefield scope. The cortex was excited by a blue LED light source (Thorlabs, M470L3, λ=470 nm). which was focused on the cortical surface with the objective (NA 0.6, MVL25M23, Navitar). Emitted light was collected with 1x magnification two-lens systems (NA 0.6, MVL25M23, Navitar) onto a monochrome CCD camera (1500M-GE, Thorlabs). The acquisition was done with 800×800 pixels, at the frame rate of 20 Hz. A large computer display (Fig. 1(A)) was placed in front of awake head-fixed mice for presenting visual stimuli. To maximize the visual field to be mapped, the plane of display was positioned perpendicular to the plane of the retina at a 30-degree angle

Biomedical Optics EXPRESS

relative to the body axis of the animal. To generate a visual retinotopic sign map, animals were exposed to a periodically drifting (with a period of 12 seconds) bar containing flickering black-and-white checkerboard (Fig. 1(B)). Brain activity was imaged and all six visual areas with their boundaries obtained by the retinotopic map were overlaid on the surface blood vessel image (Fig. 1(C)-(D)). We used the same data processing pipeline as described in other studies [34]. Specifically, we first extracted the phase information in the calcium responses at the stimuli frequency (1/12 Hz). This is useful to remove variations in the responses due to non-visual stimuli component [35]. Second, we calculated averaged phase responses to all four cardinal directions (left, right, up and down). The difference between responses to opposite movement directions was calculated to compensate for onset latency of visual response [35]. This procedure yielded two latency-corrected phase responses maps, one for azimuth, and one for elevation. Third, we calculated the two-dimensional gradient map from each of these responses map. The angle at every pixel in the gradient maps corresponds to the direction with the steepest change in phase response locked to the changing direction of visual stimuli. Last, we took the sine of angle difference between azimuth angle map and elevation angle maps. This gives the final 'sign' map [9] which we used for defining the border of primary and higher order visual areas.

2.3. Laser ablation experiments

To determine the EAL of the visual cortex and other visual areas, laser ablation at 1300 nm at 1 kHz repetition rate was performed. The laser beams were raster scanned at a single depth below the pia surface for the duration of one frame, namely 20 s (0.05 fps), using a pair of galvanometric mirrors. For the targeted ablation field of view of 50 µm and 512×512 pixel rate, minimum number of overlapping pulses resulted in 10 s of ablation duration with a 1.3 µm $1/e^2$ one-photon lateral resolution.

Since EAL is defined as an effective attenuation length for each region, we can model light attenuation in the brain with EAL and Beer-Lambert's law as follows:

$$F = \frac{E_{surf} \exp\left(\frac{-z}{EAL}\right)}{\pi w_0^2} \tag{1}$$

where E_{surf} is the laser energy at the surface, z is the ablation depth, EAL is the effective attenuation length of cortex, w_0 is the one-photon $1/e^2$ radius at the focal plane which can be calculated from the three-photon point-spread function [19], and F is the fluence at the focal plane. To calculate the threshold fluence and EAL, Eq. (1) can be reorganized as follows:

$$E_{th,surf} = F_{th} \pi w_0^2 \exp\left(\frac{z}{EAL}\right) \tag{2}$$

By taking the natural logarithm of both sides in Eq. (2), a linear regression can be applied to calculate F_{th} and EAL:

$$\ln(E_{th,surf}) = \ln(F_{th} \pi w_0^2) + (z/EAL) \tag{3}$$

Threshold energy ($E_{th,surf}$) for each depth is calculated by fitting percent of damage with respect to applied energy on the surface. This fitting function is represented as follows [39]:

$$Damage(\%) = 50 \left[1 + erf\left(\frac{E - E_{th,surf}}{1.05 \Delta E}\right)\right] \tag{4}$$

After determining threshold energy for each depth, a linear regression was applied to ablating four different depths in V1 and each of the other visual areas.

Biomedical Optics EXPRESS

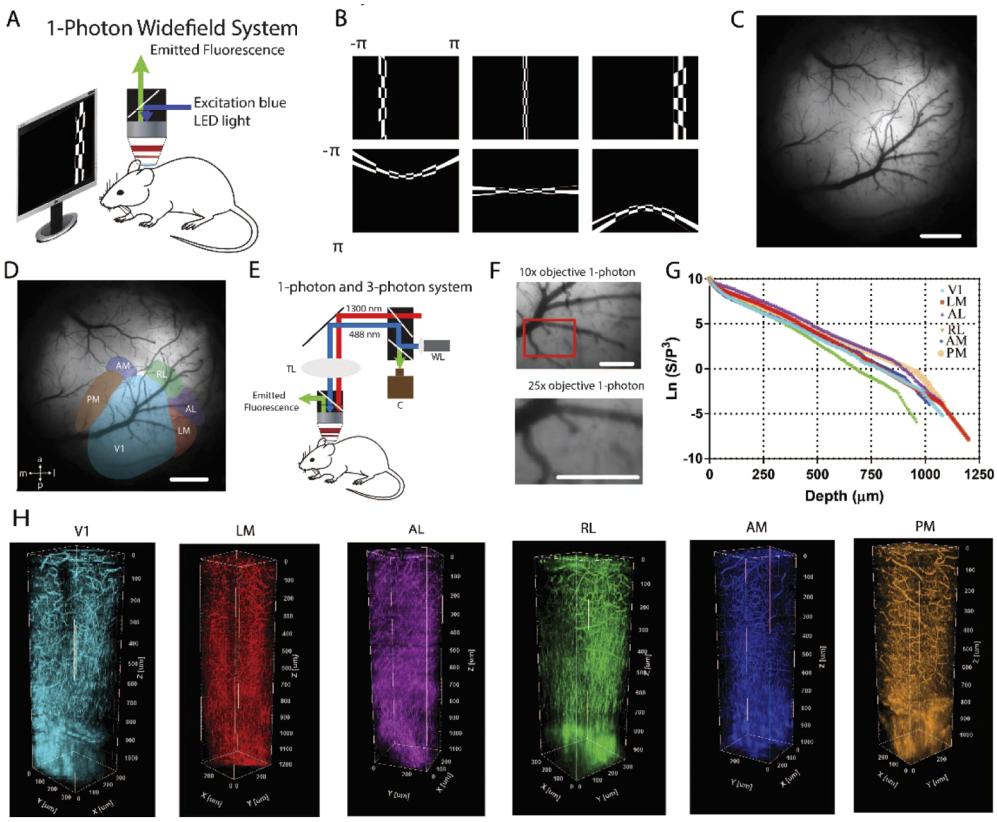

Fig. 1. (A) One-photon imaging system to obtain retinotopic maps of visual areas. Blue light was used to excite GCaMP6s in the brain of awake head-fixed mice. Emitted light (green) was collected by the camera. (B) Vertical and horizontal bars (containing flickering black and white checkerboards, and corrected for screen distance and curvature) were drifted across the screen and used to map visual areas of the cortex. (C) Blood vessel architecture of an example mouse with cranial window in the right hemisphere. (D) Representation of six cortical visual areas overlaid on the blood vessel architecture. (E) Combined one- and three-photon system to perform depth-resolved THG imaging. (F) Low magnification (10x) and high magnification (25x) images of V1 obtained with one-photon imaging system coupled with three-photon imaging system. (G) Semi-logarithmic plot for ratio of PMT signal (S) and cube of laser power (P) with respect to imaging depth for third harmonic generation (THG) imaging. Slope of this curve provides EAL values for the cortex and for the white matter. As the slope increases (decreases), EAL value decreases (increases). (H) Three-dimensional rendering of a sequence of >200 lateral THG images acquired with 5-μm increment. THG signal is generated in the blood vessels in the cortex and is generated in myelin fibers in the white matter. Each color represents a different visual area. Scale bars present 1 mm in (C-D), and 0.5 mm in (F).

Biomedical Optics EXPRESS

2.4. Calculation of combined EAL for the cortex and the white matter

After calculating EALs for the cortex and the white matter, we can define a single *EAL* (EAL_{comb}) which combines these two *EAL*s as follows:

$$E_{surf}\exp\left[-\left(\frac{t_{ctx}+t_{wm}}{EAL_{comb}}\right)\right]=E_{surf}\exp\left[-\left(\frac{t_{ctx}}{EAL_{ctx}}+\frac{t_{wm}}{EAL_{wm}}\right)\right] \tag{5}$$

where t_{ctx} and t_{wm} are the thicknesses of the cortex and the white matter, respectively. Similarly, EAL_{ctx} and EAL_{wm} are the *EAL*s of the cortex and the white matter, respectively. To calculate the EAL_{comb}, Eq. (5) can be reorganized as follows:

$$EAL_{comb}=\frac{EAL_{ctx}EAL_{wm}(t_{ctx}+t_{wm})}{(t_{ctx}EAL_{wm})+(t_{wm}EAL_{ctx})} \tag{6}$$

2.5. Quantification of cell size and density

Low magnification images of brain slices were taken with a 10x magnification objective (Olympus). We performed tiling in lateral directions, and depth-resolved imaging with 10 μm increment in the axial direction, followed by maximum intensity projection to register the final image to the Allen Brain Atlas using a custom algorithm [40]. Then, we located each visual area and acquired high magnification images with a 20x magnification objective (Olympus) with 1 μm increment in the axial direction. Finally, we performed maximum intensity projection and applied the "Analyze Particles" module in Image J to quantify the cell size and cell density for each visual area.

2.6. Relationship between scattering length and cytoarchitecture of visual areas

From Mie theory, the scattering length (ℓ_s) of biological tissues can be calculated as follows [22]:

$$\ell_s=\frac{1}{\mu_s}=\frac{1-g}{\mu_s'}=\frac{1-g}{\frac{3\phi(1-\phi)}{4a}3.28\left(\frac{2\pi a n_{ex}}{\lambda}\right)^{0.37}(m-1)^{2.09}} \tag{7}$$

where μ_s is scattering coefficient, μ_s' is reduced scattering coefficient, g is average cosine of the scattering angle, $\emptyset$ is the volume fraction or cell density, a is the radius of the cell, λ is the wavelength of the light, m=(n_{in}/n_{ex}) is the refractive index of the intracellular and extracellular fluid, respectively. We can calculate scattering length of each visual area by taking $n_{ex}=1.33$ and $m=1.04$ as determined previously [22]. Then, we can combine the scattering lengths of each visual area with the absorption length of water (ℓ_a) at 1300 nm [41] to calculate *EAL* values as follows:

$$EAL=\left(\frac{1}{\ell_s}+\frac{1}{\ell_a}\right)^{-1} \tag{8}$$

2.7. Quantification of orientation of blood vessels and myelin fibers

To quantify the orientation of blood vessels in the cortex and the orientation of myelin fibers in the white matter, we performed depth-resolved THG imaging with 1 μm increment in the axial direction. With this fine incremental imaging, we could calculate the orientation of small blood vessels and myelin fibers via Imaris software. Imaris software provided an orientation map spanning from -180° to +180°; we converted this map to a range of 0 to +180°.

2.8. Image analysis for imaging and ablation experiments

After acquiring THG images at multiple depths, the average intensity of 2% of the brightest pixel intensities was calculated for each THG image. Then, these average intensities for each image

Biomedical Optics EXPRESS

was used to plot the THG intensity distribution as a function of the imaging depth (Fig. 1(G)). Finally, the slope of this distribution was used to calculate the EAL values for each visual area.

An image analysis algorithm was developed to calculate percent of damage in the GCaMP6s images. First, a median filter with a size of 2×2 was applied to smooth the images. Otsu's thresholding method [42] was applied to remove background noise and to convert the images into binary ones. Then, the percent of damage was calculated by taking the ratio of difference of total number of pixels below the threshold before and after in ablation images to the total number of pixels corresponding to the targeted ablation area.

2.9. Surgical procedures

Experiments were carried out under protocols approved by MIT's Animal Care and Use Committee and conformed to NIH guidelines. All data in this study were collected from adult (>8 weeks old) mice of either sex. The mouse line was created by crossing Ai93 (TITLa-tTa) with Emx1-IRES-Cre mice lines from The Jackson Laboratory. Mice were initially anesthetized with 4% isoflurane in oxygen and maintained on 1.5-2% isoflurane throughout the surgery. Buprenorphine (1 mg/kg, subcutaneous) and/or meloxicam (1 mg/kg, subcutaneous) was administered preoperatively and every 24 h for 3 days to reduce inflammation. Ophthalmic ointment was used to protect the animal's eyes during the surgery. Body temperature was maintained at 37.5 °C with a heating pad. The scalp overlying the dorsal skull was sanitized and removed. The periosteum was removed with a scalpel and a craniotomy (5 mm) was made over the primary visual cortex (V1, 4.2 mm posterior, 3.0 mm lateral to Bregma) on either the left or right hemisphere, leaving the dura intact. For calcium imaging, a circular cover glass (5 mm, Warner Instruments) was implanted over the craniotomy as a cranial window, and sealed with dental acrylic (C&B-Metabond, Parkell) mixed with black ink to reduce light transmission. Finally, a custom-designed stainless steel head plate (eMachineShop.com) was affixed to the skull using dental acrylic. Experiments were performed at least 5 days after head plate implantation to allow animals to recover. For labeling blood vessels with a fluorescent dye, a Rhodamine + Dextran dye (Thermofisher, 70kDa, D1841) mixed with Saline solution at 5% w/v concentration was applied retroorbitally with 100 µl volume [43]. During the retroorbital injection, the animal was anesthetized with 2% isoflurane in oxygen. During multiphoton imaging, the animal was anesthesized with Ketamine + Xylazine mixture with 0.1 ml volume and this mixture was applied as needed after checking the reflexes. The imaging sessions lasted for a maximum of 2 hours.

2.10. Histology

Animals were deeply anesthetized with 4% isoflurane and perfused transcardially with 0.1 M phosphate-buffered saline (PBS) followed by chilled 4% paraformaldehyde in 0.1 MPBS. The brains were then postfixed in 4% paraformaldehyde in 0.1 M PBS (<4 °C) overnight. The fixed brains were sectioned into 100 µm slices with a vibratome and then mounted on a glass slide with Vectashield Hardset Antifade Mounting Medium with DAPI (Vector Labs). The slides were imaged using a confocal microscope (Leica TCS SP8).

2.11. Statistics

EAL values in cortex and white matter of visual areas were compared using one-way ANOVA with multiple comparisons (Fig. 3). One-factor ANOVA (or Watson-Williams test) in MATLAB circular statistics toolbox was applied to the data presented in Fig. 6. Specifically, we compared the circular mean values between pairs of visual areas (Fig. 6(C) and 6(F)), and between one visual area with multiple visual areas such as V1 to AM and PM (Fig. 6(C)) or V1 to LM, RL, and PM (Fig. 6(F)).

Biomedical Optics EXPRESS

3. Results

3.1. Calculation of effective attenuation lengths via two label-free methods in six visual areas in awake mice

We first determined the retinotopic mapping of cortical areas for each animal with the use of one-photon microscopy in mice expressing GCaMP6s calcium indicator (Fig. 1(A), see Methods). By drifting a bar containing a checkerboard visual stimulus from –180 to 180 degrees in both azimuthal and altitude directions, we could reliably distinguish six visual areas - V1, PM, AM, RL, AL, and LM (Fig. 1(B)-(D), see Visualization 1 and Visualization 2). Taking the blood vessel architecture and retinotopic map as a reference, we utilized a custom-made three-photon microscope [19] (Fig. 1(E)-(F)) to perform depth-resolved THG imaging at 1300 nm in each cortical region, including the cortex and white matter spanning >1 mm thickness (Fig. 1(H), see Visualization 3 for fly through depth-resolved THG images of the six visual cortical areas). Then, we characterized the attenuation of THG signal with respect to imaging depth for each region to calculate their EAL for the cortex and the white matter (Fig. 1(G)). Larger slopes represent lower EAL (such as in area RL), whereas smaller slopes represent higher EAL (such as in area PM). We calculated three EAL values for each area (cortex-only, white matter-only, and the combination of the cortex and the white matter) in eight awake mice. In each visual area, we imaged one field of view (FOV) in random locations. Since both lateral and medial visual areas are smaller than V1, our FOV is mostly located around the center of these higher visual areas.

All of these EAL values showed similar trends across all animals (Fig. 3(A-C)). PM and AM had the highest EAL values in the cortex compared to other visual areas, whereas LM and RL had the smallest EAL values in the cortex (Fig. 3(A)). When we considered EAL values in the white matter, LM, RL, and PM had lower EAL values than those in V1, AL, and AM (Fig. 3(B)). Finally, when we combined EAL values in the cortex and the white matter as a single EAL value (EAL_{comb}), LM and RL had still lower EAL values compared to those in other areas (Fig. 3(C)). Thus, these results indicate systematic changes in EAL values between cortical areas and representations, suggesting that there are structural differences between functionally distinct visual areas in awake mice.

To evaluate whether THG imaging of blood vessels and myelin fibers at 1300 nm can be used to effectively estimate EAL values, we performed ablation to four depths in the same cortical column in each cortical area. Ablation-based measurements are an alternative, commonly used method that had been used in previous studies to estimate EALs and does not depend on the emission wavelength. We compared our THG imaging results with ablation results in V1 (Fig. 2). First, we calculated EAL values in the cortex and in the white matter by characterizing the attenuation of THG signal at 1300 nm (Fig. 2(A)). The slopes of these curves resulted in 259.7 ± 14.6 µm EAL for the cortex and 104.5 ± 4.4 µm EAL for the white matter. To apply the ablation method in awake mouse cortex, four different depths ranging from 150 to 600 µm in 150 µm increments were ablated. A characteristic plot showing percent ablation versus laser energy at brain surface (Fig. 2(B)) for 150 µm ablation depth showed that 30.0 nJ pulse energy on the surface was required to obtain 50% ablation, where the targeted ablation diameter was 25 µm. To calculate the percent of ablation damage, GCaMP6s and THG images were obtained before and after ablation with varying pulse energies from 10 to 70 nJ. The slope of the threshold energy (Eth) versus ablation depth (Fig. 2(C)) corresponded to 299.6 ± 17.4 µm extinction length, while the y-axis intercept provided a threshold fluence of 1.44 ± 0.13 J/cm^2. We also performed ablation experiments in other visual areas (see. Figures 9–13 in the Appendix) and concluded that EAL values obtained with ablation experiments are 17 ± 3% higher than those obtained with THG imaging (Fig. 2(D)). Importantly, the relative EAL values were highly consistent between the two measurements. This comparison also showed the clustering of EAL values of medial (PM, AM) areas and lateral areas (RL, LM, and AL) (Fig. 2(D)). Medial regions had higher EAL

Biomedical Optics EXPRESS

values (> 300 µm for THG, >350 µm for ablation) than those in lateral areas (<275 µm for THG, and <300 µm for ablation). These results first show that the EAL values can be estimated reliably with THG imaging of blood vessels and myelin fibers. Also, these results suggest that EAL values of medial and lateral areas differ from each other which may be due to their structural differences.

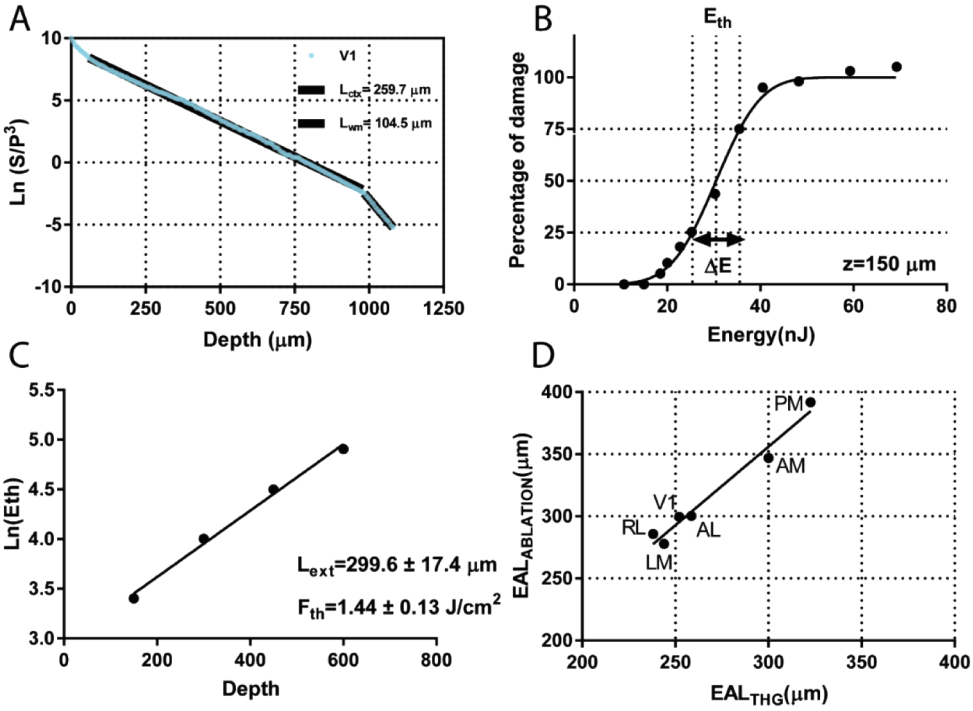

Fig. 2. Characterization of EAL values via THG imaging and ablation in V1. (A) THG imaging in V1 results in 259.7 ± 14.6 µm effective attenuation length for the cortex and 104.5 ± 4.4 µm effective attenuation length for the white matter. (B) Determining extinction length via tissue ablation. Percent of damage ranges from 0 to 100% with respect to laser energy on the tissue surface. Threshold energy (Eth) is the energy which results in 50% damage. For ablation at 150 µm depth, Eth is 30.0 nJ. (C) Semi-logarithmic plot of threshold energies for 4 different depths results in attenuation length of 299.6 ± 17.4 µm and threshold fluence of 1.44 ± 0.13 J/cm^2. (D) Comparison of EAL values obtained with THG imaging and ablation. Lateral cortical regions such as LM, AL, and RL have lower EAL values compared to those in medial regions such as AM and PM.

3.2. EAL values of visual areas exhibit similar trends as retinotopic sign maps

The boundaries of visual areas were determined by generating their visual field sign map where each visual area has a modulo sign value of -1 or 1. In this sign map, each region has an opposite sign compared to the sign of the regions adjacent to it and with which it shares a significant border - flipped signs reflect mirror-image representations in adjacent areas with a common border [7,36,44]. Thus, the sign of V1 is reversed in its adjacent regions with a significant border (LM, RL, PM). AL has a flipped sign with respect to LM and RL, whereas AM has a flipped sign with respect to PM. These sign flips can be arbitrarily represented in order as: V1 (+), LM (-), AL (+), RL (-), AM (+), and PM (-). We examined whether our EAL values were unique to each region and significantly different from regions next to each other (Fig. 3).

Biomedical Optics EXPRESS

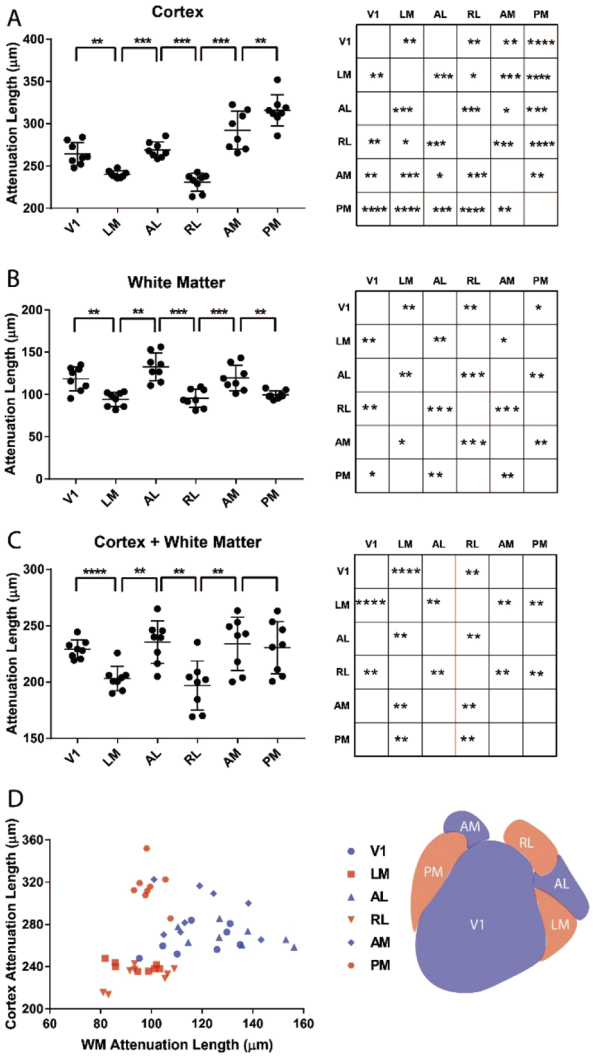

Fig. 3. Comparison of EAL values via THG imaging across visual areas in eight animals. (A) Comparison of EAL values in the cortex of visual areas (left); p values of one-way ANOVA test with multiple comparisons for EAL values of cortex across all visual areas (right). * represents $p<0.05$, ** represents $p<0.01$, *** represents $p<0.001$, and **** represents $p<0.0001$. (B) Comparison of EAL values in the white matter of visual areas (left); p values of one-way ANOVA test with multiple comparisons for EAL values of the white matter across all visual areas (right). (C) Comparison of EAL values of combined cortex and white matter of visual areas (left); p values of one-way ANOVA test with multiple comparisons for EAL values of the combination of cortex and white matter across all visual areas (right). (D) Comparison of EAL values via THG imaging in the cortex and in the white matter across visual areas in eight animals. Scatter plot of EAL values in the cortex and in the white matter of six visual areas provides clustering of these regions. Inset: Retinotopic map of six visual areas where the sign of each region is represented by either blue or red. Blue represents three regions (V1, AM, AL) with + sign; red represents three regions (PM, RL, LM) with - sign.

Biomedical Optics EXPRESS

First, we found that V1 has a significantly different EAL value than any other region except AL (Fig. 3(A)). Many of the other regions also had different EAL values compared to other regions. For example, LM has a significantly different EAL than other regions except RL (Fig. 3(A), right). Thus, the EAL is potentially a unique marker of most of the medial and lateral visual cortical areas considering their visual map sign values. Importantly, we observed significant differences in EAL values between regions adjacent to each other in the order mentioned above (Fig. 3(A), right). Furthermore, the EAL values showed the same trend as the sign maps, so that areas with positive sign had higher EALs than areas with negative sign (Fig. 3(A), left). The trend was particularly apparent when we compared EAL values in regions next to each other. The only exception occurred between AM and PM where AM had a lower EAL value than PM (Fig. 3(A), left).

Next, we compared EAL values in the white matter and found that there was a significant difference in EAL values between regions next to each other (Fig. 3(B), right). Importantly, there was a continuous decrease and increase in EAL values from V1 to PM. In other words, V1, AL, and AM had significantly higher EAL values than LM, RL, and PM, respectively (Fig. 3(B), left). These changes thus followed a similar trend as the functional retinotopic sign map in all six cortical areas. Since the EAL values in the white matter is an end result of orientation and density of myelin fibers, we may conclude that similar to human and non-human primate brain morphology, visual areas in the mouse brain have different myelin morphology.

We compared the combined EAL values of the cortex (see Methods and Materials) and the white matter since they showed different EAL patterns between AM and PM areas. There was a significant difference in EAL values between regions next to each other except between AM and PM (Fig. 3(C), right). More importantly, there was a continuous flip in the gradient of these EAL values from V1 to PM (Fig. 3(C), left). The average EAL of the cortex-only, white matter-only, and combination of the cortex and white matter for the six visual areas are tabulated in Table 1. Although the combined EAL values showed a similar trend with the retinotopic sign map of six visual areas, the EAL values in AM and PM were not significantly different from each other (Fig. 3(C), right). The reason why there is no significant difference in combined EAL values of these two areas is that AM has lower cortex and higher white matter EAL values than those in PM so that these two opposite significantly different trends cancel each other. Therefore, the combined EAL values in AM and PM regions are not significantly different from each other although these values in the white matter and the cortex are significantly different from each other (Fig. 3(A)-(B), right).

Table 1. Mean effective attenuation lengths (EAL) for cortex-only, white-matter only, and combination of cortex and white matter across eight awake mice

Length (μm) /Area	V1	LM	AL	RL	AM	PM	S1
EAL_{ctx}	264.3	240.2	269.1	230.7	292.3	315.9	310.2
EAL_{wm}	118.5	94.2	132.8	95.4	119.5	99.5	108.7
EAL_{comb}	229.1	203.3	235.6	196.9	234.1	230.6	244.2

Finally, we compared attenuation lengths of each region in the cortex and in the white matter for each animal (Fig. 3(D)). This comparison demonstrated clustering of brain regions with the same sign in the retinotopic map: LM, RL, and PM formed a cluster with low white matter EAL values whereas V1, AL and AM formed a cluster with high white matter EAL values. In some of these eight animals,V1 and AM EAL values were located between these two clusters but overall most of EAL values of positive sign visual areas (19/24 data points in Fig. 3(D)) have higher white matter EAL values than those of negative sign visual areas. These findings clearly suggest that EAL values of the white matter can be a better identifier to differentiate these visual areas. In addition to the white matter EAL values, cortex EAL values can be good identifier to differentiate

Biomedical Optics EXPRESS

medial and lateral brain regions in the mouse brain. Most of the medial regions (AM and PM, 11/16 data points in Fig. 3(D)) have higher cortex EAL values than those of the lateral regions.

3.3. EAL values in the primary cortex show heterogeneity

Since primary visual cortex (V1) is significantly larger than other visual areas and some of the cortex and white matter V1 measurements (Fig. 3(D)) are aligned with the measurements in the visual areas with opposite sign of V1, we would like to investigate how EAL values change at different locations of V1. For this purpose, we imaged 7 different locations in V1 (one in the center, one in the anterior, one in the posterior, two in the lateral, and another two in the medial locations) either in the right (Animal #7) or in the left (Animal #8) hemisphere of an awake mouse brain (Fig. 4).

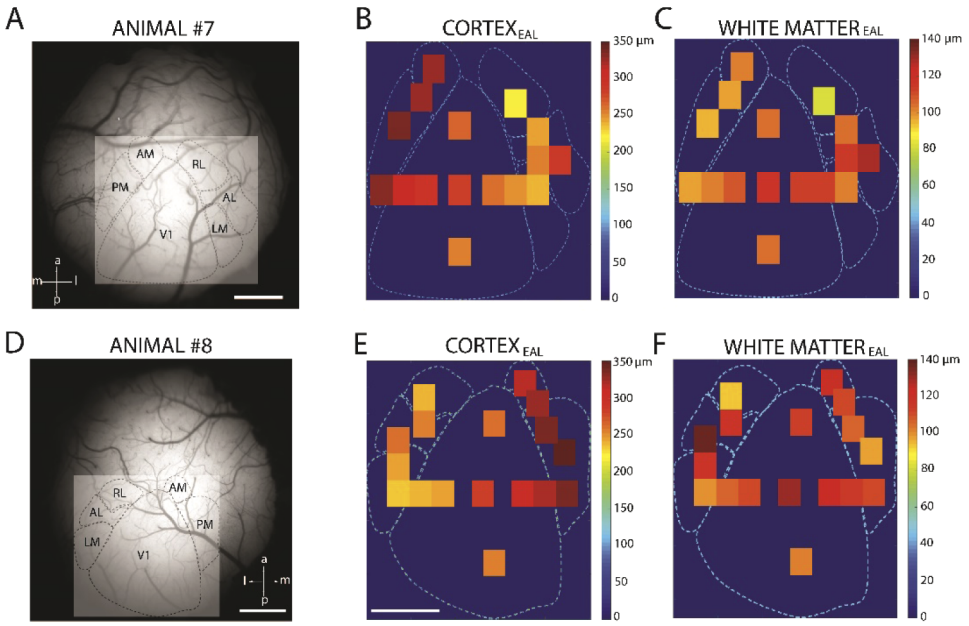

Fig. 4. Comparison of EAL values of visual areas in the left and right hemisphere of the awake mouse brain. (A) Blood vessel architecture overlaid with the boundaries of six visual areas of a mouse #7 with cranial window in the right hemisphere. (B) EAL values in the cortex of six visual areas of mouse #7 shows gradual changes from lateral to medial regions in V1 as well as at the boundaries of adjacent visual areas. (C) EAL values in the white matter of six visual areas of mouse #7 shows gradual changes from center to medial and lateral regions in V1 as well as at the boundaries of adjacent visual areas. (D) Blood vessel architecture overlaid with the boundaries of six visual areas of a mouse #8 with cranial window in the left hemisphere. (E) EAL values in the cortex visual areas of mouse #8 shows gradual changes from lateral to medial regions in V1 as well as at the boundaries of adjacent visual areas. (F) EAL values in the white matter of six visual areas of mouse #8 shows gradual changes from center to medial and lateral regions in V1 as well as at the boundaries of adjacent visual areas. Scale bars are 1 mm.

When we considered the cortex EAL values in V1, we found that the values had an increasing trend from lateral to medial regions of V1 for both animal #7 and #8 (Fig. 4(B), (E)). However, we did not find significant differences in the EAL values of anterior and posterior regions of the V1 in both animals. Interestingly, we found another trend in the EAL values of white matter in both animals (Fig. 4(C), (F)). EAL values in the white matter were highest in the center of the V1

Biomedical Optics EXPRESS

and they had a decreasing trend when we moved our imaging FOV from its center to anterior, posterior, medial or lateral regions in both mice. Since white matter EAL values of PM (in the medial side of V1) and LM (in the lateral side of V1) were significantly lower than those in the central side of V1, it makes sense that EAL values in V1 are decreasing when we move our focus from center to lateral or medial directions. Overall, central portion of V1 has higher EAL values in the white matter compared to those values in LM and PM. Also, central part of V1 has higher (lower) values in the cortex compared to those values in LM (PM). Therefore, the EAL values in the cortex and in the white matter of V1 approach similar values of medial and lateral visual areas as we move our FOV closer to these areas. Finally, we conclude that V1 measurements which are aligned with the measurements of minus sign visual areas were performed closer to LM and PM (Fig. 3(D)).

3.4. EAL values change gradually at the boundary of visual areas

Since there is a heterogeneity in the EAL values of V1 as well as there is a significant difference in EAL values of adjacent visual areas, it is important to investigate whether there is a gradual or an abrupt change in the EAL values at the boundaries of visual areas. Thus, we imaged FOVs on the area borders between V1-LM, LM-AL, AL-RL, AM-PM and PM-V1. Since we also imaged FOVs on both sides of the area borders, we could decipher whether there was a gradual or an abrupt change in the EAL values while moving our FOV from one visual area to another. For this purpose, we calculated the slope of cortex and white matter EAL values from the center of V1 to both LM and PM regions in both animal #7 and #8 (Fig. 7 in the appendix). Figure 7 shows that there is no significant difference in the slope of cortex and white matter EAL values within V1 and across the border of V1-LM and V1-PM. These results support our conclusion that there is a gradual transition rather than sharp transition in EAL values between two adjacent visual areas (Fig. 4). When we considered EAL values in the cortex, we found that there was a decreasing trend as we moved our FOV from V1 to LM, AL to RL, and PM to V1 whereas there was an increasing trend as we moved our FOV from LM to AL, and AM to PM. Similarly, when we considered EAL values in the white matter, we found that there was a decreasing trend as we moved our FOV from V1 to LM, AL to RL, and AM to PM whereas there was an increasing trend as we moved our FOV from LM to AL, and PM to V1.

3.5. Cytoarchitecture, myeloarchitecture, and blood vessel architecture of visual areas can estimate their EAL values

We first characterized the cell size and cell density of these visual areas in order to describe their cytoarchitecture. We sacrificed each animal after THG imaging, sliced their brains, and registered each coronal sections to the Allen Brain Atlas using a custom algorithm [40]. With this algorithm, we could compensate any errors due to tilt of the coronal sections in low-magnification images. Then, we performed high-magnification imaging in individual visual areas (Fig. 5(A)) and quantified the average cell size and cell density (see Methods and Materials) (Fig. 5(B)). We estimated the scattering length of each region by using their average cell size and density values via a numerical model [22] (see Methods and Materials). To estimate the EAL values for each region, we combined the scattering lengths with the absorption length of water at 1300 nm [41]. Comparing the estimated EAL values with the experimental values for the same mouse (Fig. 5(C)) showed that the estimate of EAL values from the cytoarchitecture of these visual areas agreed well with experimental EAL values obtained with THG imaging in the cortex. This result suggests that one of the structural substrates that affects the EAL value of each visual area is its cytoarchitecture.

We also investigated the in vivo myeloarchitecture and blood vessel architecture of these visual areas to see whether they were correlated with EAL values and the retinotopic sign map. We performed depth-resolved THG imaging with finer step size (1 μm) in the axial direction to

Biomedical Optics EXPRESS

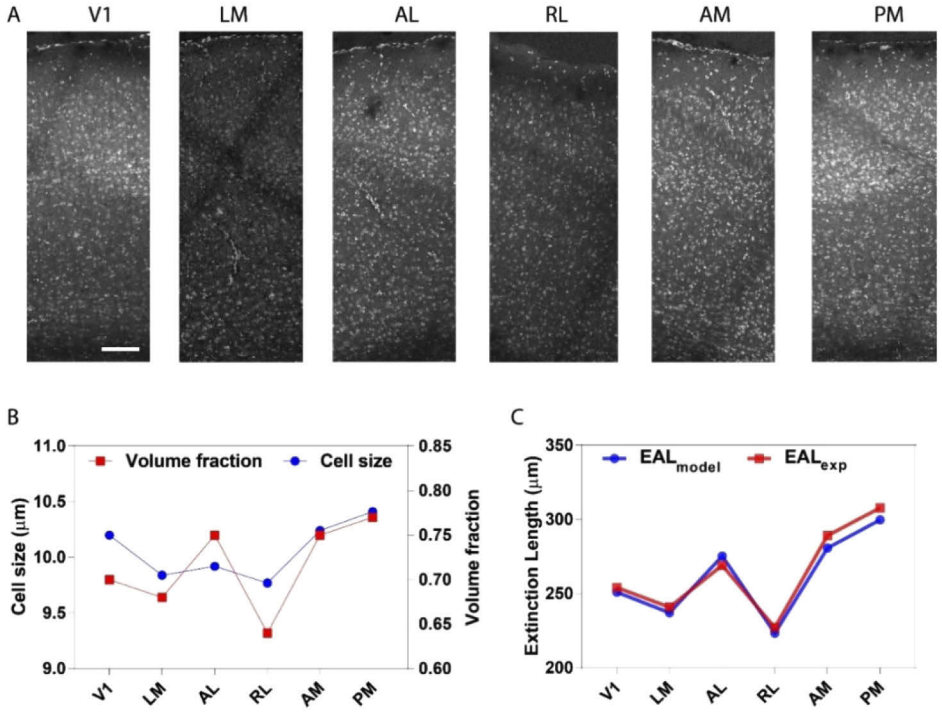

Fig. 5. Quantification of cell size and volume fraction, and estimate of effective attenuation length (EAL). (A) High magnification images of cortical column cytoarchitecture of the six cortical areas. (B) Quantification of average cell size and volume fraction for all six visual areas. (C) Comparison of experimental and theoretical EAL values.

calculate the orientation of blood vessels and myelin fibers with respect to the same horizontal direction in the cortex and in the white matter (Fig. 6(A)). First, we analyzed the orientation of the blood vessels in the cortex and demonstrated the distribution of their orientation in polar plots for each region (Fig. 6(B)). To determine whether the distribution of blood vessel orientation in each visual area was significantly different from others, we applied a circular multi- sample one-factor ANOVA statistical test (Fig. 6(C)) (see Methods and Materials). This analysis revealed that blood vessel orientation distributions in AM and PM were significantly different than orientation distributions in V1, LM, RL, and AL (see Visualization 4 and Visualization 5 for fly through images of blood vessel orientation in RL and AM, respectively). Furthermore, we calculated the circular mean of these orientation distributions and found that circular mean values of AM and PM regions were higher than 90° and circular mean values of V1, LM, RL, and AL regions were smaller than 90° (Fig. 6(D)). This analysis also showed that there were two clusters according to blood vessel orientation: one was composed of medial regions and the other one was formed by lateral regions and V1 (Visualization 4 and Visualization 5 show orientation of blood vessels skewed to far left and far right in RL and AM, respectively). This result agreed well with our THG imaging and ablation results where lateral regions and V1 formed a cluster of lower EAL values whereas medial regions formed a cluster of higher EAL values (Fig. 2(D)). Furthermore, this result also showed that blood vessel architecture was another important structural substrate contributing to the EAL value of each visual area.

We next analyzed the orientation of myelin fibers in the white matter (see Fig. 6(A)) and represented the distribution of their orientation in polar plots for each region (Fig. 6(E)). Similar to the blood vessel orientation analysis, we applied a circular multi-sample one-factor ANOVA

Biomedical Optics EXPRESS

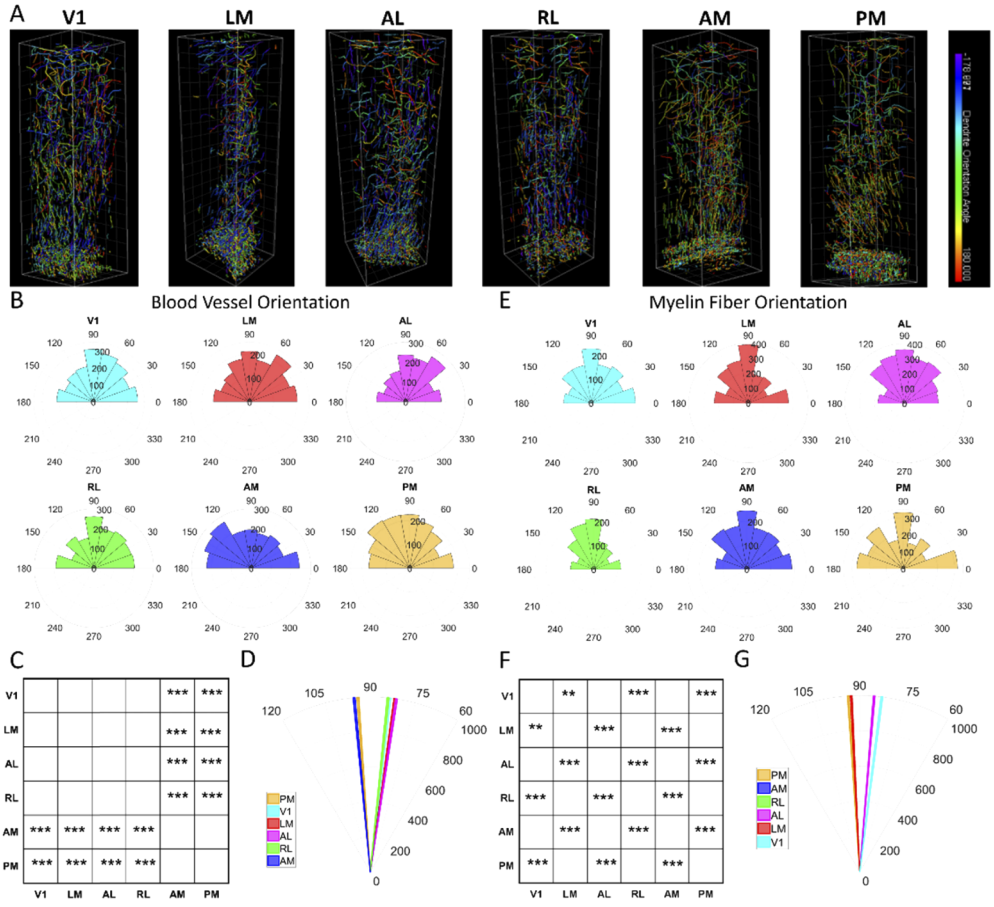

Fig. 6. Quantification of orientation of blood vessels and myelin fibers. (A) Three-dimensional depth-resolved THG images for six visual areas highlighting orientation of blood vessels in the cortex and myelin fibers in the white matter. (B) Polar plots of blood vessel orientation in six visual areas. (C) Statistical comparison of circular mean values of blood vessels. (D) Representation of circular mean values of blood vessels in polar plots. (E) Polar plots of myelin fiber orientation in six visual areas. (F) Statistical comparison of circular mean values of myelin fibers. (G) Representation of circular mean values of myelin fibers in polar plots.

statistical test on the myelin fiber orientation distribution in each visual area (Fig. 6(F)). This analysis showed that the orientations of myelin fibers in V1, AL, and AM were significantly different from those in LM, RL, and PM. We calculated the circular mean of these orientation distributions and found that circular mean values of LM, RL, and PM were higher than 90° and circular mean values of V1, AL, and AM were smaller than 90° (Fig. 6(G). Circular mean values showed that there were two clusters according to myelin fiber orientation: (i) V1, AL, and AM, (ii) LM, RL, and PM (Visualization 4 and Visualization 5 show the orientation of myelin fibers in regions RL and AM skewed to far left and far right, respectively). This result also agreed with our THG imaging results in the white matter where the regions with the same sign in retinotopic maps had similar EAL values (Fig. 3(B)): specifically, V1, AL, and AM had higher EAL values, whereas LM, RL, and PM had smaller EAL values. These results suggest that myeloarchitecture

Biomedical Optics EXPRESS

in the white matter is also an important structural substrate to have a strong correlation with EAL values.

To check whether there was a significant overlap between THG signal and fluorescence signal from the blood vessels in the cortex and the white matter, we labeled blood vessels with Rhodamine + Dextran mixture (see Methods and Materials). Then, we acquired Rhodamine + Dextran signal as well as THG signal in the V1 of an anesthetized mouse at 1300 nm excitation wavelength. We found that there was a significant overlap between THG signal and Rhodamine + Dextran signal in the cortex (Fig. 8(A-C) in the Appendix) whereas there was no significant overlap between these signals in the white matter (Fig. 8(D-E)). In addition to comparing the overlap between these two signals, we also checked how similar the three-dimensional orientation of blood vessels (BV) acquired by Rhodamine + Dextran signal and THG signal in the cortex and in the white matter. First, we compared their orientation in the cortex and we found that their orientation are significantly similar ($p=0.7284$, one-way ANOVA test, Fig. 8(F), first and second column from the left) which shows that our orientation results with THG imaging agree with those acquired with Rhodamine + Dextran based fluorescence imaging. Then, we compared three-dimensional orientation results in the white matter and we found that THG imaging and Rhodamine + Dextran imaging results are significantly different from each other ($p<0.0001$, one-way ANOVA test, Fig. 8(F), first and second column from the right). Thus, the blood vessel orientation does not affect the myelin fiber orientation results in the white matter significantly.

4. Conclusion and discussions

In this study, we sought for the first time to identify structural and functional relationship between six visual areas in awake mice by using THG microscopy, a label-free and a sub-cellular resolution three-photon microscopy technique. We compared EAL values of V1 and higher visual areas by performing label-free THG imaging of blood vessels and myelin fibers in the cortex and in the white matter as well as by performing ablation at four depths in each region. Our first key finding was that most lateral and medial cortical areas had a unique EAL; furthermore, there was a significant difference in EAL values between cortical regions adjacent to each other, and these values exhibited a pattern similar to that of the sign flip observed in the retinotopic sign map. The differences in EAL values may be explained by the following: (i) there may be differences in the size, shape, and density of cells (cytoarchitecture of neurons, astrocytes, etc.) in these cortical regions, (ii) the morphology (orientation) of blood vessels and myelin fibers may be different in these regions. Our cytoarchitecture analysis coupled with numerical estimates of EAL values in the cortex showed that there was strong agreement between our experimental EAL values and their numerical estimates. Thus, the EAL may be used as a structural metric for a cortical area, which can be obtained via in vivo imaging.

Next, we quantified the morphology of blood vessels and myelin fibers with THG imaging for each cortical region, to examine whether there was any relationship between the orientation of blood vessels and myelin fibers in these regions. These data showed that medial regions and lateral regions were significantly different from each other. Interestingly, the orientation of myelin fibers resulted in the same trend as the retinotopic sign map. This result recapitulates the coupling of structure and function of brain regions obtained with diffusion tensor imaging (DTI) of white matter tracts in human and non-human primates [3,45,46]. Overall, the morphology of blood vessels, myelin fibers, and cells showed that significant morphological differences exist between cortical areas. Structural differences between primary and higher visual areas, including cell size, density [2], as well as myelin density [45,46] have been reported in monkeys and humans. To the best of our knowledge, we show for the first time morphological differences in V1 and higher visual areas in mice, in terms of cell size and density in brain sections as well as orientation of blood vessels and myelin fibers obtained in awake conditions. These differences, which likely lead to significant differences between EAL values in these areas, are also reflected in

Biomedical Optics EXPRESS

the sign of their retinotopic map. Therefore, our study shows for the first time that structural and functional coupling of visual areas in the mouse brain can be detected at sub-cellular resolution in vivo - by combining one-photon and three-photon imaging. This advance should enable similar studies of structural and functional coupling in other sensory and non-sensory cortical areas in the brains of mice and other animal models. Importantly, with the progressive availability of wide-field one-, two- and three-photon imaging systems, further studies are required to focus on creating whole brain EAL and functional maps. With these advances, we believe that the structural and functional correlation in visual areas that we describe for the first time points to crucial developmental mechanisms that set up these areas; thus our work would lead to a better fundamental understanding of brain development, and of disorders such as Alzheimer's, stroke, and aging.

Why might the retinotopic sign map correlate with structural features of cortex as reflected in the EAL? Adjacent visual areas likely arise from a common border which represents a cardinal axis of visual space (the vertical meridian or the horizontal meridian of the contralateral visual field) [7,47]. During development, thalamocortical fibers may align themselves from this border and follow molecular gradients that confer topography [38,48]. Cortical areas with one sign (V1, AL, AM) may all represent similar thalamocortical (or intracortical) fiber orientations compared to areas with the opposite sign (RL, LM, PM). These fiber orientations would then be reflected in the orientations of myelin and even blood vessels [21,49,50] as measured with THG imaging that contribute to EALs. Since the THG signal mostly arises from the myelin fibers (thalamocortical fibers) in the white matter, we believe that EAL values mostly represent the myelin fiber structure in the white matter. However, blood vessels are not the only constituents of the cortex so that the EAL values in the cortex may not present full structure of the cortical regions. Further studies are required to address this hypothesis.

An important finding from our study was that EAL values obtained with ablation experiments were $17 \pm 3\%$ higher than EAL values obtained with THG imaging of blood vessels and myelin fibers. The main advantage of ablation is that it only relies on the excitation wavelength. However, powerful lasers are required to create lesions at multiple depths. On the other hand, the main advantage of THG imaging is that it provides realistic EAL values without using any exogenous labeling, but it still has the disadvantage of using both excitation and emission photons to estimate the EAL. The 17% difference between THG imaging results and ablation results may be due to fact that the emission photons centered at 433 nm can create an inner filter effect while we are collecting them in the PMTs. In other words, some of these emission photons, especially in deeper regions of the brain, may be absorbed in the brain tissue before they reach to the detectors. As an alternative, we could use higher excitation wavelength so that emission photons can be centered around 550-600 nm with 1700nm excitation wavelength. In this case, we most probably could not image the blood vessels with THG imaging modality. Another alternative method is to use fluorescent dyes again with higher excitation wavelengths such as 1700nm. In this case, we may have saturation and photobleaching of the fluorophore which may also affect the precision of EAL measurements. To compare our THG imaging results with previous studies based on exogenous labeling of blood vessels, we also performed THG imaging in the somatosensory cortex (S1) of awake mice where the EAL was reported as 315-330 μm [26]. Our THG results showed an EAL of 312.7 ± 2.1 μm in the cortex and 105.4 ± 1.1 μm in the white matter (Fig. 14). The agreement between our THG imaging results, ablation results, as well as blood vessel imaging results in the literature [26] suggests that the EAL of cortical regions, particularly for comparison in the same animal, can be estimated reasonably well by performing label-free THG imaging at 1300 nm excitation wavelength.

Although we performed a label-free columnar imaging of six visual areas in awake mice to characterize their EAL values via THG microscopy for the first time, a caveat of our study is that characterizing the EAL values for all six areas is a time-consuming process. Performing the

Biomedical Optics EXPRESS

columnar imaging for each visual area takes approximately 15 minutes with 5 μm increment in the axial direction. Therefore, it takes 1-2 hours to obtain the columnar imaging data in these six visual areas. With the development of wide-field and multi-plane three-photon microscopy systems, we believe that this whole imaging process will take less than 10 minutes in the near future. In addition, we can hypothesize that there may be significant differences in EAL values of other brain regions such as prefrontal cortex, motor cortex, and auditory cortex compared to visual areas as long as they have a significant change in their cytoarchitecture, myeloarchitecture and blood vessel architecture. Of course, further studies are required to check this hypothesis.

Appendix

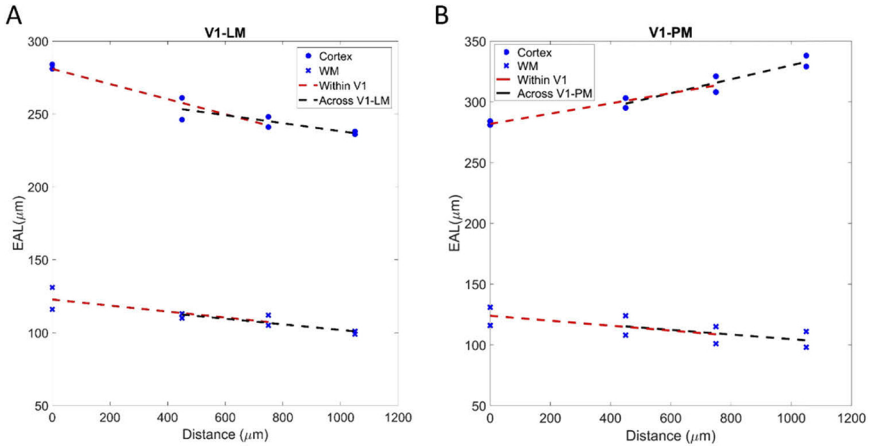

Fig. 7. Gradual change of EAL values in the cortex and in the white matter between the center of V1(distance=0 μm) to LM and PM. (A) The changes in the slope of EAL values in the cortex (p=0.1149) and in the white matter (p=0.9001) within V1 (red dashed lines) and across the border of V1-LM (black dashed lines) are not significant for both Animal #7 and #8. (B) The changes in the slope of EAL values in the cortex (p=0.2679) and in the white matter (p=0.9527) within V1 (red dashed lines) and across the border of V1-PM (black dashed lines) are not significant for both Animal #7 and #8.

Biomedical Optics EXPRESS

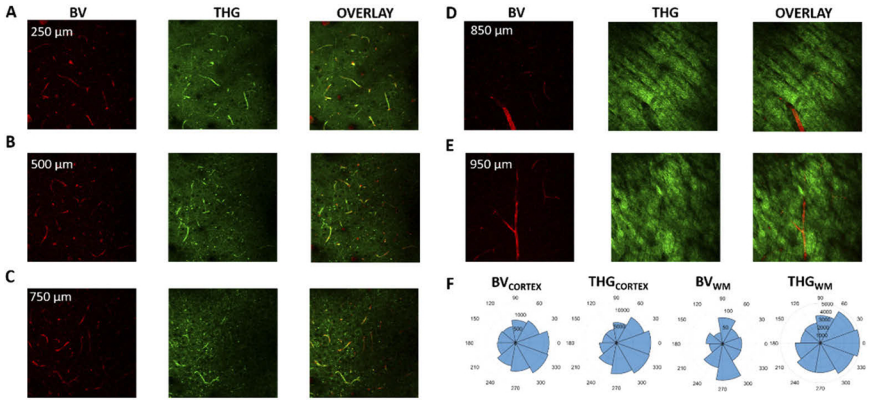

Fig. 8. Comparison between Rhodamin-Dextran mixture (red) and THG signal (green) in the cortex and in the white matter. Rhodamin-Dextran mixture mostly labels the blood vessels (BV) both in the cortex and white matter, and THG signal also mostly labels blood vessels in the cortex and myelin fibers in the white matter (WM). (A,B,C) Representative images at multiple depths in the cortex (250, 500 and 750 µm depths) shows significant overlap (right column) between blood vessel (BV, left column) fluorescence images and THG (middle column) images. (D,E) Representative images at two different depths (850 and 950 µm) in the white matter shows that THG signal and the blood vessel fluorescence signal do not overlap with each other. (F) Orientation of blood vessel fluorescence signals and THG signals in the cortex are significantly similar to each other (first and second column from the left) whereas their orientation values are significantly different in the white matter (last two columns from the right).

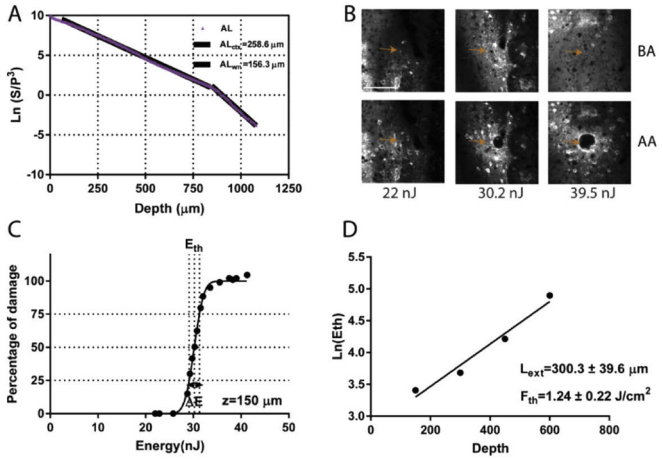

Fig. 9. Characterization of EAL values via THG imaging and ablation in AL. (A) THG imaging in AL results in 258.6 ± 10.4 µm effective attenuation length for the cortex and 156.3 ± 9.5 µm effective attenuation length for the white matter. (B) Representative images before ablation (BA) and after ablation (AA) for three pulse energies (22, 30.2 and 39.5 nJ) at 150 µm depth. Arrows show the location of target region for the ablation before and after applying laser pulses for each pulse energy. (C) Determining extinction length via tissue ablation. Percent of damage ranges from 0 to 100% with respect to laser energy on the tissue surface. Threshold energy (E_{th}) is the energy which results in 50% damage. For ablation at 150 µm depth, E_{th} is 30.2 nJ. (D) Semi-logarithmic plot of threshold energies for 4 different depths results in attenuation length of 300.3 ± 39.6 µm and threshold fluence of 1.24 ± 0.22 J/cm^2.

Biomedical Optics EXPRESS

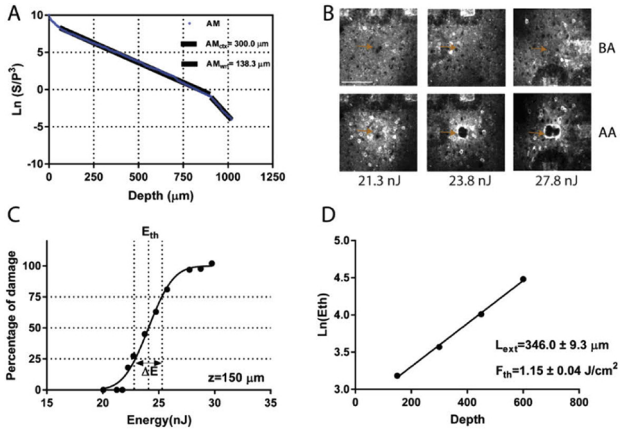

Fig. 10. Characterization of EAL values via THG imaging and ablation in AM. (A) THG imaging in AL results in 300.0 ± 11.9 μm effective attenuation length for the cortex and 138.3 ± 4.5 μm effective attenuation length for the white matter. (B) Representative images before ablation (BA) and after ablation (AA) for three pulse energies (21.3, 23.8 and 27.8 nJ) at 150 μm depth. Arrows show the location of target region for the ablation before and after applying laser pulses for each pulse energy. (C) Determining extinction length via tissue ablation. Percent of damage ranges from 0 to 100% with respect to laser energy on the tissue surface. Threshold energy (E_{th}) is the energy which results in 50% damage. For ablation at 150 μm depth, E_{th} is 24.1 nJ. (D) Semi-logarithmic plot of threshold energies for 4 different depths results in attenuation length of 346.0 ± 9.3 μm and threshold fluence of 1.15 ± 0.04 J/cm^2.

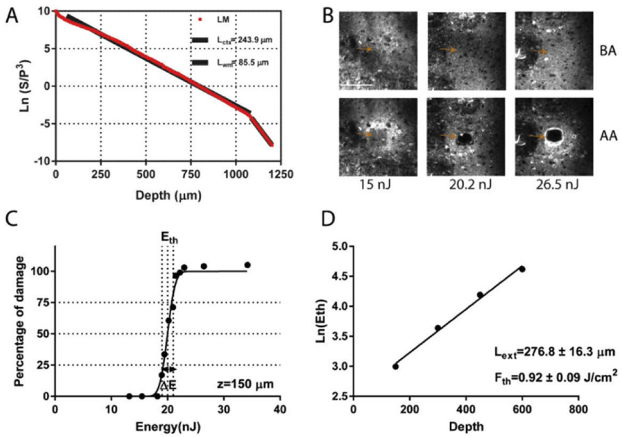

Fig. 11. Characterization of EAL values via THG imaging and ablation in LM. (A) THG imaging in AL results in 243.9 ± 11.2 μm effective attenuation length for the cortex and 85.5 ± 3.5 μm effective attenuation length for the white matter. (B) Representative images before ablation (BA) and after ablation (AA) for three pulse energies (15, 20.2 and 26.5 nJ) at 150 μm depth. Arrows show the location of target region for the ablation before and after applying laser pulses for each pulse energy. (C) Determining extinction length via tissue ablation. Percent of damage ranges from 0 to 100% with respect to laser energy on the tissue surface. Threshold energy (E_{th}) is the energy which results in 50% damage. For ablation at 150 μm depth, E_{th} is 20 nJ. (D) Semi-logarithmic plot of threshold energies for 4 different depths results in attenuation length of 276.8 ± 16.3 μm and threshold fluence of 0.92 ± 0.09 J/cm^2.

Biomedical Optics EXPRESS

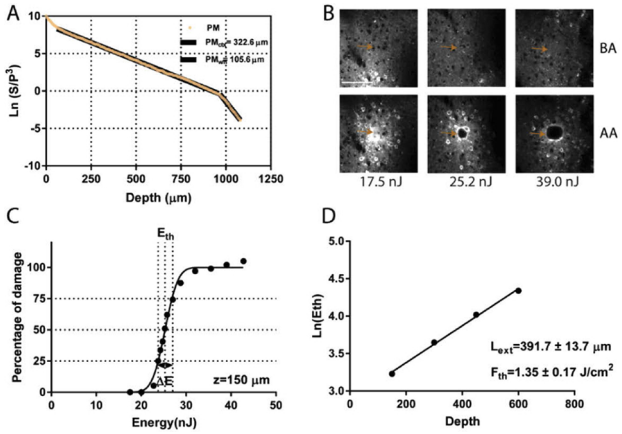

Fig. 12. Characterization of EAL values via THG imaging and ablation in PM. (A) THG imaging in AL results in 322.6 ± 14.5 µm effective attenuation length for the cortex and 105.6 ± 4.3 µm effective attenuation length for the white matter. (B) Representative images before ablation (BA) and after ablation (AA) for three pulse energies (17.5, 25.2 and 39.0 nJ) at 150 µm depth. Arrows show the location of target region for the ablation before and after applying laser pulses for each pulse energy. (C) Determining extinction length via tissue ablation. Percent of damage ranges from 0 to 100% with respect to laser energy on the tissue surface. Threshold energy (E_{th}) is the energy which results in 50% damage. For ablation at 150 µm depth, E_{th} is 25.3 nJ. (D) Semi-logarithmic plot of threshold energies for 4 different depths results in attenuation length of 391.7 ± 13.7 µm and threshold fluence of 1.35 ± 0.17 J/cm^2.

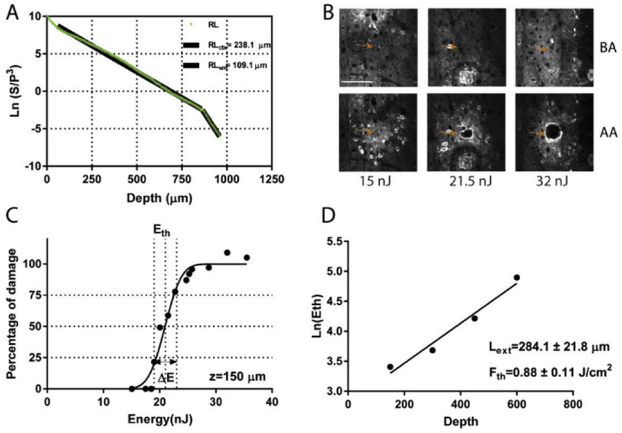

Fig. 13. Characterization of EAL values via THG imaging and ablation in RL. (A) THG imaging in AL results in 238.1 ± 14.0 µm effective attenuation length for the cortex and 109.1 ± 2.9 µm effective attenuation length for the white matter. (B) Representative images before ablation (BA) and after ablation (AA) for three pulse energies (15, 21.5 and 32.0 nJ) at 150 µm depth. Arrows show the location of target region for the ablation before and after applying laser pulses for each pulse energy. (C) Determining extinction length via tissue ablation. Percent of damage ranges from 0 to 100% with respect to laser energy on the tissue surface. Threshold energy (E_{th}) is the energy which results in 50% damage. For ablation at 150 µm depth, E_{th} is 21.0 nJ. (D) Semi-logarithmic plot of threshold energies for 4 different depths results in attenuation length of 284.1 ± 21.8 µm and threshold fluence of 0.88 ± 0.11 J/cm^2.

Biomedical Optics EXPRESS

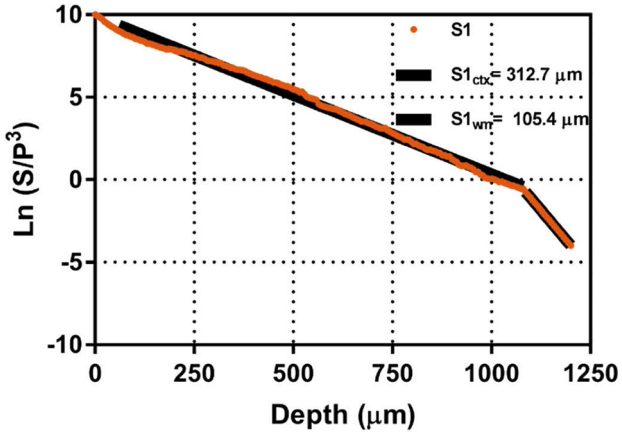

Fig. 14. Characterization of EAL values via THG imaging in S1. THG imaging in S1 results in 312.7 ± 2.1 µm effective attenuation length for the cortex and 105.4 ± 2.1 µm effective attenuation length for the white matter. Raw data is in orange, linear fits are in black.

Funding

National Institutes of Health (4-P41-EB015871, EY007023, EY028219, K99EB027706); National Science Foundation (EF1451125).

Acknowledgments

This work was supported by US National Institute of Health (NIH) grants EY007023 and EY028219 (MS), 4-P41-EB015871 (PTCS), K99EB027706 (MY), US National Science Foundation (NSF) grant EF1451125 (MS), a Picower Institute Engineering Collaboration Grant (MS, MY and PTCS), and an equipment grant from the Massachusetts Life Sciences Initiative.

Disclosures

The authors declare no conflicts of interest.

References

1. E. Bullmore and O. Sporns, "Complex brain networks: graph theoretical analysis of structural and functional systems," Nat. Rev. Neurosci. **10**(3), 186–198 (2009).
2. C. E. Collins, D. C. Airey, N. A. Young, D. B. Leitch, and J. H. Kaas, "Neuron densities vary across and within cortical areas in primates," Proc. Natl. Acad. Sci. U. S. A. **107**(36), 15927–15932 (2010).
3. M. F. Glasser, M. S. Goyal, T. M. Preuss, M. E. Raichle, and D. C. Van Essen, "Trends and properties of human cerebral cortex: Correlations with cortical myelin content," NeuroImage **93**, 165–175 (2014).
4. M. F. Glasser and D. C. Van Essen, "Mapping human cortical areas in vivo based on myelin content as revealed by T1- and T2-weighted MRI," J. Neurosci. **31**(32), 11597–11616 (2011).
5. M. J. Brookes, M. Woolrich, H. Luckhoo, D. Price, J. R. Hale, M. C. Stephenson, G. R. Barnes, S. M. Smith, and P. G. Morris, "Investigating the electrophysiological basis of resting state networks using magnetoencephalography," Proc. Natl. Acad. Sci. U. S. A. **108**(40), 16783–16788 (2011).
6. M. D. Fox and M. E. Raichle, "Spontaneous fluctuations in brain activity observed with functional magnetic resonance imaging," Nat. Rev. Neurosci. **8**(9), 700–711 (2007).
7. M. I. Sereno, A. M. Dale, J. B. Reppas, K. K. Kwong, J. W. Belliveau, T. J. Brady, B. R. Rosen, and R. B. Tootell, "Borders of multiple visual areas in humans revealed by functional magnetic resonance imaging," Science **268**(5212), 889–893 (1995).
8. J. D. Cohen, W. M. Perlstein, T. S. Braver, L. E. Nystrom, D. C. Noll, J. Jonides, and E. E. Smith, "Temporal dynamics of brain activation during a working memory task," Nature **386**(6625), 604–608 (1997).
9. M. I. Sereno, C. T. McDonald, and J. M. Allman, "Analysis of retinotopic maps in extrastriate cortex," Cereb. Cortex **4**(6), 601–620 (1994).

Biomedical Optics EXPRESS

10. K. Amunts, A. Schleicher, and K. Zilles, "Cytoarchitecture of the cerebral cortex–more than localization," NeuroImage **37**(4), 1061–1065 (2007).
11. S. B. Eickhoff, K. E. Stephan, H. Mohlberg, C. Grefkes, G. R. Fink, K. Amunts, and K. Zilles, "A new SPM toolbox for combining probabilistic cytoarchitectonic maps and functional imaging data," NeuroImage **25**(4), 1325–1335 (2005).
12. R. D. Fields, "A new mechanism of nervous system plasticity: activity-dependent myelination," Nat. Rev. Neurosci. **16**(12), 756–767 (2015).
13. E. M. Gibson, D. Purger, C. W. Mount, A. K. Goldstein, G. L. Lin, L. S. Wood, I. Inema, S. E. Miller, G. Bieri, J. B. Zuchero, B. A. Barres, P. J. Woo, H. Vogel, and M. Monje, "Neuronal activity promotes oligodendrogenesis and adaptive myelination in the mammalian brain," Science **344**(6183), 1252304 (2014).
14. S. Pajevic, P. J. Basser, and R. D. Fields, "Role of Myelin Plasticity in Oscillations and Synchrony of Neuronal Activity," Neuroscience **276**, 135–147 (2014).
15. M. F. Glasser, T. S. Coalson, E. C. Robinson, C. D. Hacker, J. Harwell, E. Yacoub, K. Ugurbil, J. Andersson, C. F. Beckmann, M. Jenkinson, S. M. Smith, and D. C. Van Essen, "A multi-modal parcellation of human cerebral cortex," Nature **536**(7615), 171–178 (2016).
16. A. F. Atik, E. Calabrese, R. Gramer, S. M. Adil, S. Rahimpour, P. Pagadala, G. A. Johnson, and S. P. Lad, "Structural mapping with fiber tractography of the human cuneate fasciculus at microscopic resolution in cervical region," NeuroImage **196**, 200–206 (2019).
17. K. Svoboda, W. Denk, D. Kleinfeld, and D. W. Tank, "In vivo dendritic calcium dynamics in neocortical pyramidal neurons," Nature **385**(6612), 161–165 (1997).
18. K. Svoboda, F. Helmchen, W. Denk, and D. W. Tank, "Spread of dendritic excitation in layer 2/3 pyramidal neurons in rat barrel cortex in vivo," Nat. Neurosci. **2**(1), 65–73 (1999).
19. M. Yildirim, H. Sugihara, P. T. C. So, and M. Sur, "Functional imaging of visual cortical layers and subplate in awake mice with optimized three-photon microscopy," Nat. Commun. **10**(1), 177 (2019).
20. D. G. Ouzounov, T. Wang, M. Wang, D. D. Feng, N. G. Horton, J. C. Cruz-Hernandez, Y. T. Cheng, J. Reimer, A. S. Tolias, N. Nishimura, and C. Xu, "In vivo three-photon imaging of activity of GCaMP6-labeled neurons deep in intact mouse brain," Nat. Methods **14**(4), 388–390 (2017).
21. M. J. Farrar, F. W. Wise, J. R. Fetcho, and C. B. Schaffer, "In vivo imaging of myelin in the vertebrate central nervous system using third harmonic generation microscopy," Biophys. J. **100**(5), 1362–1371 (2011).
22. H. Liu, B. Beauvoit, M. Kimura, and B. Chance, "Dependence of tissue optical properties on solute-induced changes in refractive index and osmolarity," J. Biomed. Opt. **1**(2), 200–211 (1996).
23. F. Helmchen and W. Denk, "Deep tissue two-photon microscopy," Nat. Methods **2**(12), 932–940 (2005).
24. M. Oheim, E. Beaurepaire, E. Chaigneau, J. Mertz, and S. Charpak, "Two-photon microscopy in brain tissue: parameters influencing the imaging depth," J. Neurosci. Methods **111**(1), 29–37 (2001).
25. J. M. Stujenske, T. Spellman, and J. A. Gordon, "Modeling the Spatiotemporal Dynamics of Light and Heat Propagation for In Vivo Optogenetics," Cell Rep. **12**(3), 525–534 (2015).
26. M. Wang, C. Wu, D. Sinefeld, B. Li, F. Xia, and C. Xu, "Comparing the effective attenuation lengths for long wavelength in vivo imaging of the mouse brain," Biomed. Opt. Express **9**(8), 3534–3543 (2018).
27. Y. Barad, H. Eisenberg, M. Horowitz, and Y. Silberberg, "Nonlinear scanning laser microscopy by third harmonic generation," Appl. Phys. Lett. **70**(8), 922–924 (1997).
28. M. Muller, J. Squier, K. R. Wilson, and G. J. Brakenhoff, "3D microscopy of transparent objects using third-harmonic generation," J. Microsc. **191**(3), 266–274 (1998).
29. N. E. Ruiz-Uribe, S. J. Ahn, and C. B. Schaffer, "Label Free Imaging of Cortical Blood Vessels Using Third Harmonic Generation (THG) Microscopy," in *Optical Molecular Probes, Imaging and Drug Delivery*, (Optical Society of America, 2019), JT4A.11.
30. E. J. Gualda, G. Filippidis, M. Mari, G. Voglis, M. Vlachos, C. Fotakis, and N. Tavernarakis, "In vivo imaging of neurodegeneration in Caenorhabditis elegans by third harmonic generation microscopy," J. Microsc. **232**(2), 270–275 (2008).
31. D. Yelin and Y. Silberberg, "Laser scanning third-harmonic-generation microscopy in biology," Opt. Express **5**(8), 169–175 (1999).
32. A. R. Jones, C. C. Overly, and S. M. Sunkin, "The Allen Brain Atlas: 5 years and beyond," Nat. Rev. Neurosci. **10**(11), 821–828 (2009).
33. G. Paxinos and K. B. Franklin, *Paxinos and Franklin's The Mouse Brain in Stereotaxic Coordinates* (Academic press, 2019).
34. M. E. Garrett, I. Nauhaus, J. H. Marshel, and E. M. Callaway, "Topography and areal organization of mouse visual cortex," J. Neurosci. **34**(37), 12587–12600 (2014).
35. V. A. Kalatsky and M. P. Stryker, "New paradigm for optical imaging: temporally encoded maps of intrinsic signal," Neuron **38**(4), 529–545 (2003).
36. J. Zhuang, L. Ng, D. Williams, M. Valley, Y. Li, M. Garrett, and J. Waters, "An extended retinotopic map of mouse cortex," eLife **6**, e18372 (2017).
37. B. D. Fulcher, J. D. Murray, V. Zerbi, and X. J. Wang, "Multimodal gradients across mouse cortex," Proc. Natl. Acad. Sci. U. S. A. **116**(10), 4689–4695 (2019).

Biomedical Optics EXPRESS

38. D. D. O'Leary, S. J. Chou, and S. Sahara, "Area patterning of the mammalian cortex," Neuron **56**(2), 252–269 (2007).
39. C. Martin and A. Ben-Yakar, "Determination of scattering properties and damage thresholds in tissue using ultrafast laser ablation," J. Biomed. Opt. **21**(11), 115004 (2016).
40. P. Shamash, M. Carandini, K. D. Harris, and N. A. Steinmetz, "A tool for analyzing electrode tracks from slice histology," bioRxiv, 447995 (2018).
41. G. M. Hale and M. R. Querry, "Optical constants of water in the 200-nm to 200-μm wavelength region," Appl. Opt. **12**(3), 555–563 (1973).
42. N. Otsu, "A threshold selection method from gray-level histograms," IEEE Trans. Syst., Man, Cybern. **9**(1), 62–66 (1979).
43. T. Yardeni, M. Eckhaus, H. D. Morris, M. Huizing, and S. Hoogstraten-Miller, "Retro-orbital injections in mice," Lab Animal **40**(5), 155–160 (2011).
44. J. H. Marshel, M. E. Garrett, I. Nauhaus, and E. M. Callaway, "Functional specialization of seven mouse visual cortical areas," Neuron **72**(6), 1040–1054 (2011).
45. R. M. Sánchez-Panchuelo, S. T. Francis, D. Schluppeck, and R. W. Bowtell, "Correspondence of human visual areas identified using functional and anatomical MRI in vivo at 7 T," Cigongzhen Chengxiang **35**(2), 287–299 (2012).
46. M. I. Sereno, A. Lutti, N. Weiskopf, and F. Dick, "Mapping the human cortical surface by combining quantitative T 1 with retinotopy," Cereb. Cortex **23**(9), 2261–2268 (2013).
47. J. H. Kaas, A. W. Roe, M. K. Baldwin, and D. C. Lyon, "Resolving the organization of the territory of the third visual area: a new proposal," Vis. Neurosci. **32**, E016 (2015).
48. T. McLaughlin and D. D. O'Leary, "Molecular gradients and development of retinotopic maps," Annu. Rev. Neurosci. **28**(1), 327–355 (2005).
49. V. Barun and A. Ivanov, "Estimate of the contribution of localized light absorption by blood vessels to the optical properties of biological tissue," Opt. Spectrosc. **96**(6), 940–945 (2004).
50. H. Lim, D. Sharoukhov, I. Kassim, Y. Zhang, J. L. Salzer, and C. V. Melendez-Vasquez, "Label-free imaging of Schwann cell myelination by third harmonic generation microscopy," Proc. Natl. Acad. Sci. U. S. A. **111**(50), 18025–18030 (2014).